



# Simultaneous integration of the photosensitizer hemin and biocatalyst nanoferrihydrite into a single protein nanocage for selectively photocatalytic CO<sub>2</sub> reduction

Ruiqi Zeng, Xiaoxi Chang, Tuo Zhang, Chenyan Lv, Jiachen Zang<sup>\*</sup>, Guanghua Zhao<sup>\*</sup>

College of Food Science & Nutritional Engineering, China Agricultural University, Beijing Key Laboratory of Functional Food from Plant Resources, Beijing 100083, China

## ARTICLE INFO

### Keywords:

Ferritin  
Heme  
Ferrihydrite  
CO<sub>2</sub> photoreduction  
Protein assembly  
Recyclability

## ABSTRACT

The artificial photoreduction of CO<sub>2</sub> into fuels with precious metal-based photosensitizers such as Ru, Re, and Ir represents a potential way to minimize global warming caused by the growing concentration of CO<sub>2</sub>, but these noble metal-based photosensitizers present unsustainable and negative environmental impact issues, thereby limiting their applications. Herein, bioinspired by the inherent ability of *Escherichia coli* ferritin (EcBFR) to bind to hemin, we constructed a photocatalytic-CO<sub>2</sub>-conversion platform by using a single shell-like EcBFR molecule where up to 12 of hemin molecules can be incorporated into its intersubunit interfaces as photosensitizers, while the semiconductor photocatalysts nanoferrihydrites are catalytically synthesized and encapsulated within the protein inner cavity. Consequently, the constructed platform can selectively, effectively reduce CO<sub>2</sub> to formic acid with 1-benzyl-1,4-dihydronicotinamide (BNAH) as the electron donor in aqueous solution under mild conditions. To improve the recyclability of the above platform, we designed a three-dimensional (3D) protein crystalline framework with the above constructed hybrid molecules as building blocks through  $\pi$ - $\pi$  interactions. Notably, such protein framework enables the recyclability to be improved up to at least 5 cycles as compared to the individual protein nanocage. All these findings pave the way for CO<sub>2</sub> photoreduction by naturally occurring heme as the photosensitizer in an environmentally friendly manner.

## 1. Introduction

Photocatalytic CO<sub>2</sub> reduction into valuable chemicals or energy carrier by solar energy has initiating an environmentally friendly route to realize carbon elimination. At present, a cornucopia of artificial photosynthesis systems has been constructed to serve highly efficient CO<sub>2</sub> photoreduction [1–3]. In a typical homogeneous photocatalytic CO<sub>2</sub> reduction system, a photosensitizer (PS) is a key component responsible for light-harvesting and photocatalytic reduction. To date, noble-metal based photosensitizers containing Ru, Re, or Ir have been mainstream in artificial photosynthesis systems [4], because they have large absorption cross sections in the visible region and are capable of promoting efficient multiple electron transfer processes. Unfortunately, expensive price and hazardous effects are two major factors driving this desire to switch from noble metal to noble metal-free systems in practical applications [5,6]. Hence, the demand for the development of light-driven CO<sub>2</sub> reduction catalysts based on earth-abundant transition metals for practical photochemical applications has been increasing.

Iron is an abundant transition element on the earth. Hemin is a macrocyclic complex of iron with the metal ion coordinated equatorially to the four nitrogen atoms of an electronically delocalized protoporphyrin IX ring, which represents the most typical porphyrin molecule [7]. Unfortunately, in an aqueous environment, the hemin molecules self-associate and aggregate to form different non-monomeric species mainly due to the hydrophobic nature of the tetrapyrrole ring, affecting the dynamical and structural properties of the hemin molecules as well as their functions, thereby limiting the application of hemin as a photosensitizer [8]. For the technical applications of hemin, diverse research groups have immobilized hemin on high surface area materials such as graphene [9], [10], and tungsten disulfide [11]. While in biological systems, hemin turns into heme through ligation to the side chains of His, Cys, Met residues and even the N-terminus of protein in much vital proteins (e.g., hemoglobin and myoglobin) and enzymatic structures such as peroxidases, mono and dioxygenases, and cytochromes [12–14]. Heme plays an important role as a cofactor of these hemoproteins and in turn the proteins endow heme with improved

<sup>\*</sup> Corresponding authors.

E-mail addresses: [zangjiachen@cau.edu.cn](mailto:zangjiachen@cau.edu.cn) (J. Zang), [gzhao@cau.edu.cn](mailto:gzhao@cau.edu.cn) (G. Zhao).

<https://doi.org/10.1016/j.apcatb.2023.123521>

Received 14 September 2023; Received in revised form 31 October 2023; Accepted 13 November 2023

Available online 17 November 2023

0926-3373/© 2023 Elsevier B.V. All rights reserved.

solubility and durability. Hence the heme bound to the protein can be a promising pathway for its use as photosensitizer. Recently, porphyrin-based complexes [15,16] or molecular materials and nano-reactors such as covalent-organic frameworks (COF) and metal-organic frameworks (MOF) [17] have been developed for the CO<sub>2</sub> capture and conversion. However, so far, heme, which represents one of the most widely occurring iron complexes, as photosensitizers instead of the above mentioned noble-metal complexes for CO<sub>2</sub> photocatalytic conversion has yet to be explored.

In an artificial photosynthesis (AP) system, photocatalytic core components are generally composed of a photosensitizer, a semiconductor catalyst and an electron donor [18]. To improve CO<sub>2</sub> photo-reduction efficiency of the AP, strong light-harvesting capacity, rapid electron separation and migration, and CO<sub>2</sub>-catalyst interaction should be fulfilled [19]. Over the past decade, significant progress has been achieved in artificially photocatalytic CO<sub>2</sub> reduction by using the above-mentioned multicomponent systems. However, inefficient electron migration based on random collision between photosensitizer and catalyst in homogeneous catalytic systems usually causes mediocre performance [20,21], resulting in the relatively low efficiency of the CO<sub>2</sub> reduction. Additionally, the discrete multicomponent systems usually have problems on controlling product selectivity [22]. Fortunately, anchoring the photosensitizers and catalysts concurrently onto MOFs or COFs can efficiently shorten the electron transfer distance and permit efficient electron injection from excited or reduced photosensitizers to adjacent catalysts, and thereby improving CO<sub>2</sub> photoreduction activity and durability [19]. Differently, in this study, we propose a hypothesis that simultaneous integration of the photosensitizer and catalyst into a single robust protein nanocage could improve CO<sub>2</sub> photocatalytic efficiency with high product selectivity through effective electron transfer between them. If so, such scaffold would be of great value for achieving durable and versatile photocatalytic systems.

On the other hand, protein nanocages are widely distributed in Nature to fulfill numerous functions such as nucleic acid storage and transport by viral capsids, endocytosis by clathrin cages, CO<sub>2</sub> fixation by carboxysomes, DNA protection by Dps, and iron metabolism by ferritin [23–25]. Recently, nanotechnologists have subverted these nature functions and explored self-assembled cage structures of nanometer dimensions as biotemplates for the preparation of inorganic and organic nanomaterials [26], and the encapsulation and delivery of guest molecules with various potential applications [27]. Although these protein nanocages have distinct functions, they share one structural feature that all of them have three distinct interfaces: the interior, the exterior and the inter-subunit interface (Fig. S1). Protein cages represent a standard structural component in ferritin. Structurally, ferritin is composed of 24 subunits assembling into a thermal-stable shell-like structure with an exterior diameter about 12 nm and a hollow cavity of 8 nm. Functionally, all known ferritins can catalyze fast Fe(II) oxidation by O<sub>2</sub> or H<sub>2</sub>O<sub>2</sub> into nanoferrihydrate iron cores and store them within its inner cavity [23]. Interestingly, bacterioferritins such as *Escherichia coli* ferritin (EcBFR) are widely distributed in a variety of prokaryotic cells, and are markedly different from animal and plant ferritins in that they can inherently bind to heme at their subunit interfaces [28,29]. All these information raises the possibility that ferritin nanocages, especially EcBFR could be explored as a new scaffold through integration of the photosensitizer and the catalyst into their two different interfaces for photocatalytic CO<sub>2</sub> reduction.

To verify the above hypotheses, here we performed a proof-of-concept study by constructing an artificial photocatalytic system with EcBFR as a protein platform based on a two-step hierarchical self-assembly procedure. First, 12 of heme molecules as photosensitizers were integrated into the C<sub>2</sub> interfaces of EcBFR under basic conditions. Second, the biocatalyst ferrihydrite nanoparticles were catalytically synthesized within the inner cavity of the heme-integrated EcBFR in an aqueous environment (pH 7.5) at 4 °C, producing the heme-integrated holo EcBFR. Consequently, hierarchical integration of the

photosensitizer heme and the catalyst ferrihydrite nanoparticles into a single EcBFR nanocage enables CO<sub>2</sub> to be selectively photoreduced to formic acid with high efficiency in the presence of BNAH under mild conditions as shown in Scheme 1. This platform represents the first case with heme as a photosensitizer for photocatalytic CO<sub>2</sub> reduction in an environmentally friendly manner.

## 2. Experimental

### 2.1. The chemicals and materials

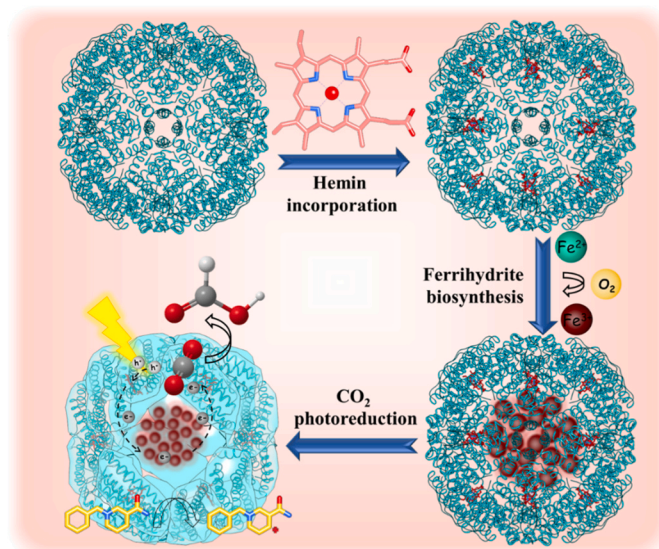
Isopropyl β-D-thiogalactoside (IPTG), ampicillin (Amp) and kanamycin sulfate (Kana) were purchased from Sigma (~99%). 2% uranyl acetate was purchased from Electron Microscopy China. 100% CO<sub>2</sub> gas was purchased from Beijing Runfeng company. Other reactants, including tris(2,2'-bipyridyl)ruthenium(II) chloride hexahydrate [Ru(bpy)<sub>3</sub>]Cl<sub>2</sub>·6 H<sub>2</sub>O, 1-benzyl-1,4-dihydropyridine (BNAH), heme chloride, and formic acid were purchased from Beijing solarbio science & technology co., ltd. All solutions were prepared with ultrapure water from a Millipore water purification system.

### 2.2. Protein expression and purification

EcBFR and its two mutants (52 H-EcBFR and 147Y-EcBFR) were expressed and purified as previously reported [28]. The purified protein solution was collected and dialyzed against 50 mM MOPS, pH 7.5, to exclude NaCl from the solution. The purified protein was concentrated with a 30 kDa molecular mass cut-off Amicon® centrifugal filter device and the protein concentrations were determined according to the Lowry method with bovine serum album as standard.

### 2.3. Heme incorporation

The purified EcBFR and its mutants 52 H-EcBFR and 147Y-EcBFR were reconstituted with heme to assure maximal occupancy of heme binding sites as previously reported with slight modifications [28,29]. Specifically, heme chloride was dissolved in 0.1 M sodium hydroxide solution, diluted with 0.15 M MOPS buffer, pH 7.5, and then centrifuged to remove insoluble material. After adding the heme solution to the



**Scheme 1.** Construction of an artificial CO<sub>2</sub> photoreduction platform by integration of the photosensitizer heme and biocatalyst nanoferrihydrate into the subunit interface and the inner cavity of EcBFR in an aqueous environment under mild conditions for photoconverting CO<sub>2</sub> to HCOOH with BNAH (highlighted in yellow) as the electron donor.

protein in 0.15 M MOPS buffer, pH 7.5, containing 1.0 M NaCl. The protein-heme mixture was incubated for 10 min at 80 °C and then cooled to room temperature. Unbound and adventitiously bound heme were removed by dialysis against buffer solution (50 mM MOPS, pH7.5) at least three times.

## 2.4. Ferrihydrite synthesis

Stock Fe(II) solutions (50 mM) were prepared in dilute anaerobic HCl, pH 2.0, solution. The purified EcBFR, 52 H-EcBFR and 147Y-EcBFR protein solutions were diluted by 50 mM MOPS buffer with pH 7.5–1.0  $\mu$ M, respectively. Subsequently, FeSO<sub>4</sub> solution was aerobically added to 20 mL of the above protein solution with a stoichiometry of Fe<sup>2+</sup>/protein = 100/1 each time at 15 min intervals to prepare ferrihydrite nanoparticles with different sizes (400 and 800 iron/shell). After standing overnight, the resultant mixture was dialyzed against 50 mM MOPS buffer with pH 7.5 for 3 times at 6 h intervals to remove free iron from the solution.

## 2.5. Sample characterizations

Hemin binding to EcBFR or its mutants was monitored by UV–vis spectroscopy. The chemical identification of ferrihydrite nanoparticles was identified by powder X-ray diffraction (XRD, Bruker D8 advance diffractometer, Cu K $\alpha$  radiation, scanning rate of 0.02 deg s<sup>−1</sup>). Their microstructures were analyzed by transmission electron microscopy (TEM, Hitachi H-7650). X-ray photoelectron spectroscopy (XPS) measurements were performed on an ESCALab MKII X-ray photoelectron spectrometer. Photoluminescence (PL) spectra was measured by using an excitation wavelength of 360 nm on an FLS 1000 fluorescence spectrophotometer. UV–vis diffuse reflectance spectra (UV–vis DRS) were determined using Thermo Nicolet Evolution 360 UV–vis spectrophotometer equipped with an integrating sphere attachment. Electron paramagnetic resonance (EPR) spectra was collected on EMX-plus EPR spectrometer at room temperature. Ultraviolet photoelectron spectroscopy (UPS) was conducted using an AXIS Supra Kratos Analytical model with a He(I) source of energy 21.2 eV, and the photoelectrons were collected with 6 eV pass energy, 0.01 eV energy step.

## 2.6. Construction of 3D protein crystalline frameworks

After heme reconstitution and ferrihydrite synthesis were finished, 147Y-EcBFR protein nanocages were used to construct 3D protein crystalline frameworks as following: 147Y-EcBFR-12Heme-800Fe was dissolved in MOPS buffer (50 mM, pH 7.5) with the protein concentration of approximately 1.0  $\mu$ M. Subsequently, aqueous MgCl<sub>2</sub> (2.0 M, pH 7.5) were added to the buffered 147Y-EcBFR-12Heme-800Fe solution to give a Mg<sup>2+</sup> concentration of 20 mM to induce individual 147Y-EcBFR-12Heme-800Fe molecules to self-assemble into 3D protein crystalline frameworks. The structure of the 3D protein crystalline frameworks was analyzed by TEM and protein X-ray crystallography.

## 2.7. Photocatalytic CO<sub>2</sub> reduction performance

Photocatalytic CO<sub>2</sub> reduction experiments were performed at room temperature using 2 mL test tube that contained 1 mL of a protein solution (5.0 mg/mL) and 0.1 M BNAH. Prior to irradiation, the suspension was purged with CO<sub>2</sub> for 30 min. A 400 W high-pressure Hg lamp ( $\lambda$  = 425 nm) was used as a light source to allow for visible-light irradiation. The gaseous products after each experiment were analyzed by gas chromatograph equipped with a thermal conductivity detector (TCD). The formic acid generated in the liquid phase was detected by continuous monitoring until 6.0 h and quantitated by HPLC on the basis of a calibration curve prepared for various concentrations of formic acid standard. HPLC method was described as below: The formic acid product was run on C-18 columns of 25 cm length, methanol and 10 mM

KH<sub>2</sub>PO<sub>3</sub> (v/v = 5:95) as mobile phase. Flow rate was used as 1.0 mL/min. Wavelength was varied between the maximum absorption spectrum of methanol (205 nm) and maximum absorption spectrum of formic acid (256 nm).

Selectivity toward formic acid production was calculated on the basis of the ratio between the amount of formic acid generated and the total amount of reduction products. The apparent quantum yield (AQY) for formic acid formation was measured using the same photochemical experimental setup. The AQY for formic acid production was calculated through the following equation: AQY % = 2 (the number of formic acid molecules)/(the number of photons)  $\times$  100%.

## 2.8. Crystallization, data collection, and structure determination

Purified proteins were concentrated to 15 mg/mL in a buffer consisting of 20 mM MOPS at pH 7.5, and crystals were obtained using the hanging drop vapor diffusion method under different conditions, which are shown in [Supplementary Table 1](#). Diffraction data were collected at the beamline BL17U and BL18U at Shanghai Synchrotron Radiation Facility (SSRF) and were processed, integrated and scaled with the HKL-3000 software [30]. Data processing statistics are shown in [Supplementary Table 2](#). The structures were determined by molecular replacement using the Molrep program in CCP4 using the structure of EcBFR (PDB code 1BFR) as a search model. Structure refinement was conducted using the Refmac5 program and PHENIX software [31]. The structure was rebuilt using COOT, which made the model manually adjusted [32]. Figures of protein structures were prepared using the UCSF Chimera package [33].

## 3. Results and discussion

### 3.1. Incorporation of the photosensitizer heme into the inter-subunit interfaces of EcBFR

Photosensitizer is mainly responsible for collecting photon energy during photocatalysis process. Among a large number of porphyrin-based photosensitizers, heme is a well-known naturally occurring photosensitizer containing four pyrrole rings joined by four methine bridges to give a near planar macrocycle, based in an 18  $\pi$ -electronic conjugated network in which iron(III) play as central metal [34]. However, tendency to undergo aggregation because of poor solubility in aqueous solution and degradation by sensitivity to oxygen and water mainly limits the application of heme itself as a photosensitizer.

Interestingly, bacterioferritin such as EcBFR differs from other ferritins by its inherent ability to bind to heme cofactors [28,29,35]. Similar to other ferritin, EcBFR naturally occurs as protein cage composed of 24 subunits with the aforementioned three chemically distinct interfaces, and the pairwise arrangement of adjacent subunits within the 24-mer creates 12 of the C<sub>2</sub> interfaces that arise specific heme-binding sites. Each subunit binds to the heme iron by coordination with Met52 to create a heme center with a highly unusual bis-methionine axial ligation as shown in [Fig. 1a](#). In order to take advantage of ameliorative heme as a photosensitizer, EcBFR was prepared by overexpression in *E. coli*, and purified protein was identified by gel electrophoresis and TEM ([Fig. S2](#)). In parallel, we also prepared an EcBFR mutant where Met52 was replaced by His, which was used as control and was referred to as 52 H-EcBFR ([Fig. S2](#)). As a result, this mutant lost the ability to bind to heme based on the fact that Met52 was vital important for incorporation of heme (see below).

Overexpressed recombinant EcBFR typically appeared scarlet, while 52 H-EcBFR was colorless ([Fig. 1b](#), inset). Indeed, UV–vis spectroscopy showed that the maximum absorption peak of the bound heme appeared at 420 nm due to coordination between heme and methionine, while free heme molecules exhibited its maximum peak at 398 nm ([Fig. 1b](#)). In contrast, no such peaks were observed with 52 H-EcBFR, suggestive of no heme binding ([Fig. 1b](#)). To confirm the above observation, we solved



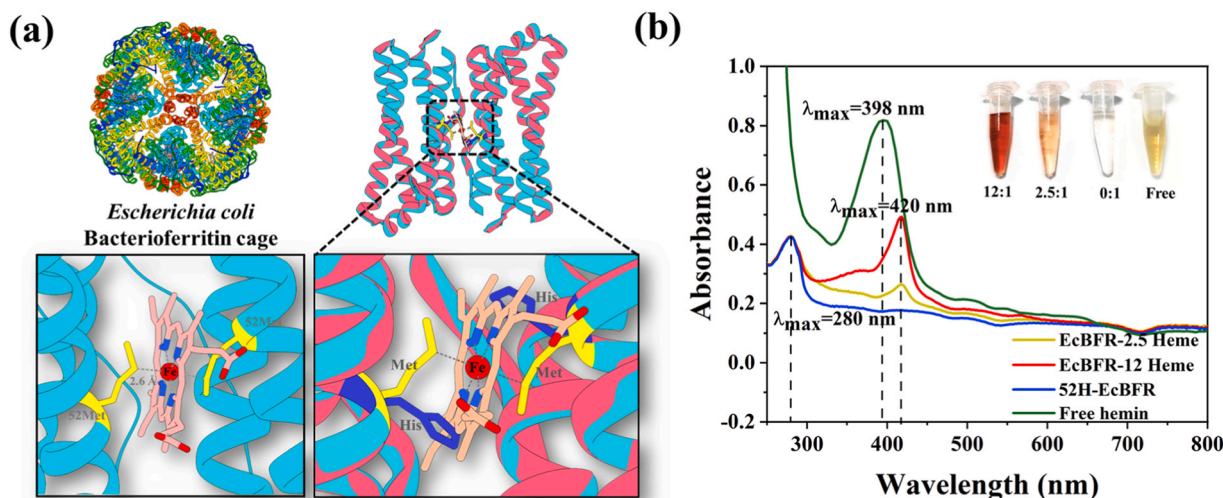


**Fig. 1.** Incorporation of heme into the inter-subunit interfaces of EcBFR. (a) Structure view of heme binding to the  $C_2$  interfaces of EcBFR through coordination with Met52 and steric hindrance from side chain of His52 preventing heme from binding in the  $C_2$  interfaces of 52 H-EcBFR. (b) UV-vis spectra of free hemin, 52 H-EcBFR, EcBFR-2.5Heme, and EcBFR-12Heme. In insert images, '12:1' and '2.5:1' represents a heme/ferritin ratio of 12/1, 2.5/1, respectively, '0:1' represents 52 H-EcBFR without heme binding, and 'free' represents only heme in solution.

the crystal structure of 52 H-EcBFR by X-ray crystallography at a resolution of 2.0 Å with 123 space group (Supplementary Tables 1 and 2), which showed that steric hindrance from the side chain of His 52 prevents heme from insertion at the inter-subunit interfaces (Fig. 1a). Thus, such crystal structure could explain the incapacitation of heme binding in the mutant 52 H-EcBFR at an atomic level.

Generally, overexpressed EcBFR contained a low level of heme, namely a heme/protein ratio of 2.5/1 was obtained as shown in Fig. 1b, which was referred to as EcBFR-2.5Heme. While addition of hemin to EcBFR solution in a high NaCl concentration at 80 °C according to a reported method [28,29] resulted in a great change in the protein electronic spectrum as demonstrated by an increase in the absorbance of the expected maximum at 420 nm (Fig. 1b). Following this treatment, all twelve of the  $C_2$  interfaces of EcBFR were occupied by heme, namely 12 molecules of heme bound to one ferritin molecule, which was termed as EcBFR-12Heme. Such a high binding quantity is conducive to heme behaving as the photosensitizer.

### 3.2. Synthesis of nanoferrihydrite as the photocatalyst within the inner cavity of EcBFR-12Heme

Exploring of a new catalyst holds a key to unlock catalytic powers of cheap and earth-abundant materials for large-scale applications. Arguably most notable within this context is the studies on the exploratory synthesis and photocatalytic property of iron based semiconductor materials [35,36]. Thanks to the nature of all ferritins, these protein can catalyze fast Fe(II) oxidation into Fe(III) by  $O_2$  or  $H_2O_2$  and encapsulate large amounts of iron ( $\leq 4500$  Fe) within their inner cavity as hydrous ferric oxide mineral cores with a structure resembling that of ferrihydrite [37]. However, so far, whether such biosynthesized ferrihydrite nanoparticles can serve as a catalyst for photocatalytic  $CO_2$  reduction remains unknown, so it is a great interest to test this idea.

To confirm this idea, we first determined the ability of EcBFR-12Heme, EcBFR-2.5Heme and the mutant 52 H-EcBFR to catalyze the formation of ferrihydrite nanoparticles, respectively, based on our previously reported method [38,39]. As expected, all of them can catalyze the oxidation of  $Fe^{2+}$  to  $Fe^{3+}$  as shown in Fig. S3a. However, incorporation of heme to EcBFR markedly inhibited iron oxidative deposition to a large extent as shown in Fig. S3b. For example, 52 H-EcBFR, which completely lost its ability to bind to heme, could catalyze the formation of ferrihydrite nanoparticles with a size of 1600 iron/protein shell in

vitro (Fig. S4), while much smaller ferrihydrite nanoparticles (800 iron/protein shell) can be catalytically prepared by EcBFR-12Heme under identical conditions (Fig. 2a), and resultant sample is referred to as EcBFR-12Heme-800Fe. At the same time, to study effect of the size of ferrihydrite nanoparticles on photocatalytic  $CO_2$  reduction (see below), the ferrihydrite nanoparticles with 400 iron/protein shell was also synthesized by using EcBFR-12Heme as a biotemplate, and resultant sample was named as EcBFR-12Heme-400Fe. For comparison, two different ferrihydrite nanoparticles (400 and 800 iron/protein shell) were likewise synthesized by 52 H-EcBFR, which were referred to as 52 H-EcBFR-400Fe and 52 H-EcBFR-800Fe, respectively.

Next, we characterized the structure of the biosynthesized ferrihydrite nanoparticles within the inner cavity of EcBFR-12Heme and 52 H-EcBFR by various physicochemical methods. Powder XRD analyses show that both EcBFR-12Heme and 52 H-EcBFR samples, which lack ferrihydrite nanoparticles within the inner cavity of protein shell, are non-crystalline, as indicated by the "bun-shaped" curves shown in Fig. 2b, upper panel. By contrast, sharp peaks were observed with other four samples (EcBFR-12Heme-400Fe, EcBFR-12Heme-800Fe, 52 H-EcBFR-400Fe and 52 H-EcBFR-800Fe) (Fig. 2b, lower panel), suggesting that ferrihydrite nanoparticles exists in these samples in crystalline form. Agreeing with this view, single crystallites regions with a lattice spacing of 2.45 Å are observed with EcBFR-12Heme-800Fe by high-resolution TEM (Fig. S5).

During ferrihydrite synthesis, the iron core of ferritin initiation could be enhanced by proximal binding of two  $Fe^{3+}$  at the nucleation center to give a bridged dimer and hydrolytic addition of further  $Fe^{3+}$  produced at the ferroxidase site in the cavity would then allow the buildup of linear and three-dimensional polymers of increasing stability [40–42]. Powder XRD analysis revealed that the synthesized ferrihydrite is an analogue of  $\alpha$ -FeOOH and  $\alpha$ -Fe $_2$ O $_3$  (Fig. 2b). The unique peaks at 15.29° and 20.25° suggest a model of ferrihydrite made up of double hexagonally closest packed oxygen atoms in a stacked lattice with the majority of iron(III) in octahedrally coordinated sites but up to 1/3 of the iron in tetrahedral sites [43,44]. Recent study proposed a single structure by analyzing the pair distribution function derived from direct Fourier transformation of total X-ray scattering, and this model structure incorporated 20% of tetrahedrally coordinated iron(III) into ferrihydrite [45–47]. The chemical state of our synthesized ferrihydrite revealed by XRD pattern is consistent with the presence of either a certain amount of tetrahedral iron or an asymmetric octahedral coordination suggested by X-ray



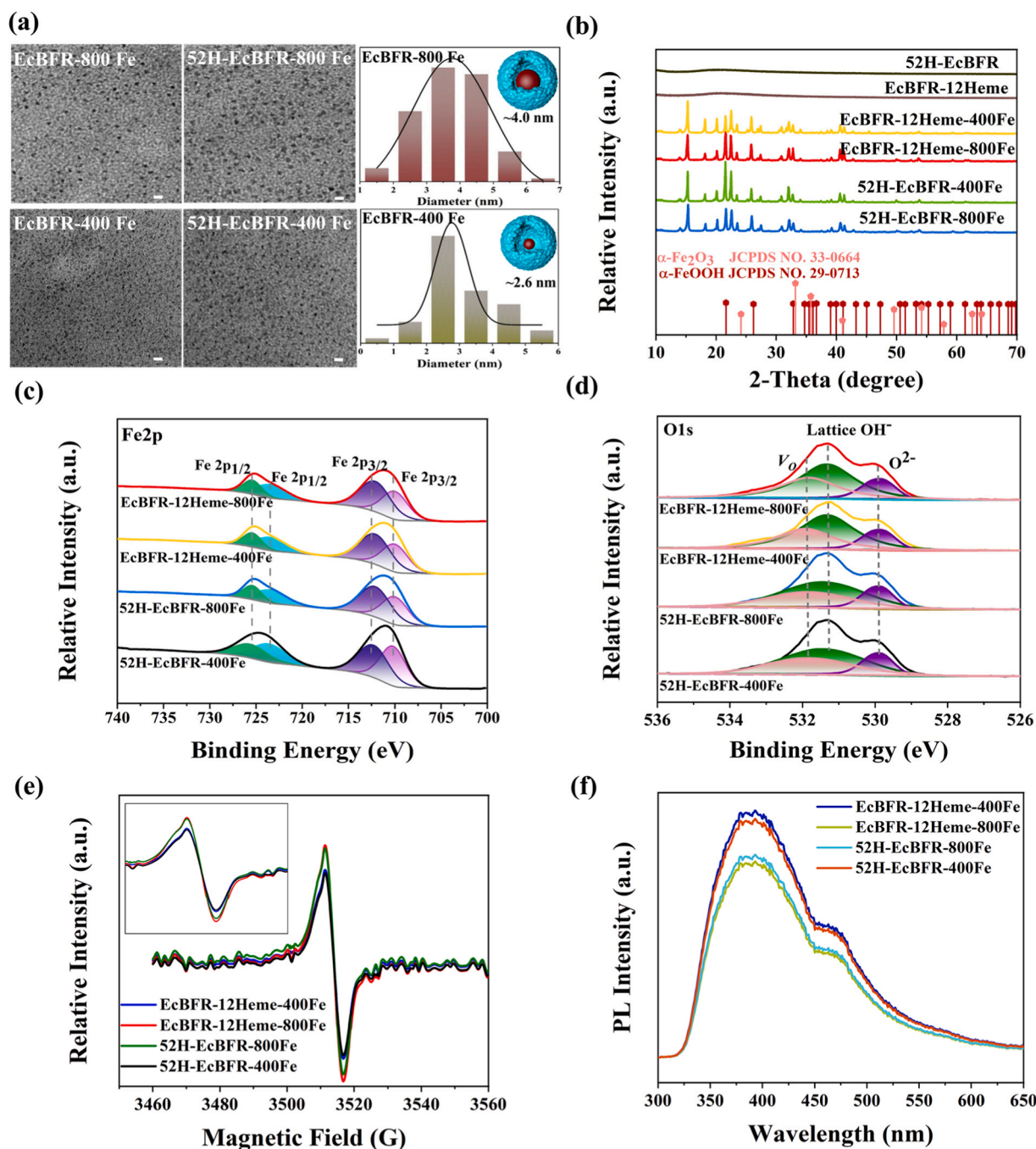


**Fig. 2.** Characterization of the biosynthesized ferrihydrite nanoparticles with different sizes within the inner cavity of EcBFR-12Heme and 52 H-EcBFR. (a) Morphological analyses and particle size distribution of ferrihydrite nanoparticles. Scale bar represent 20 nm. (b) XRD analyses of ferrihydrite nanoparticles. (c) High-resolution XPS of Fe 2p. (d) High-resolution XPS of O 1 s (e) EPR spectra of synthesized ferrihydrite nanoparticles. Inset: Magnification of the curves in the magnetic field range of 3500–3530 G. (f) Photoluminescence (PL) spectra of ferrihydrite nanoparticles with different sizes biosynthesized by EcBFR-12Heme and 52 H-EcBFR.

absorption near-edge structure (XANES) study [48,49]. The ferrihydrite nanoparticles are well embraced by intact ferritin shells so that the size of ferrihydrite is always less than 8 nm as suggested by element mapping (Fig. S6) and it shrinks gradually as the iron content decreases (Fig. 2a).

The chemical composition and electronic state of ferrihydrite were further identified by X-ray photoelectron spectroscopy (XPS) analysis. From the survey spectrum (Fig. S7a), the peaks of Fe, O, N, C and S elements can be observed and high-resolution C1 spectrum can be fitted by four major peaks that are contributed from protein shell, while the existence of C–N and C=O bonds indicates the successful deposition of ferrihydrite nanoparticles into the inner cavity of ferritin (Fig. S7b) and

this result is consistent with the above TEM analyses (Fig. 2a). In particular, the Fe 2p spectrum mainly displays two asymmetric peaks that can be deconvoluted into two doublets, one of which are located at 712.6 and 725.6 eV belonging to Fe<sup>3+</sup> ion, while another at 710.2 and 723.8 eV corresponding to Fe<sup>2+</sup> ion that is mainly attributed to the presence of oxygen vacancy (V<sub>O</sub>) in the ferrihydrite nanoparticles (Fig. 2c). Similarly, the O 1 s spectrum showed three asymmetric peaks which are located at 529.8, 531.5 and 531.8 eV, corresponding to the O<sup>2-</sup>, lattice hydroxyls and V<sub>O</sub> in the ferrihydrite nanoparticles (Fig. 2d). To further confirm the presence of V<sub>O</sub> in the ferrihydrite, the EPR spectra of samples were collected (Fig. 2e). An obvious EPR signal at g = 2.006

was observed with all ferrihydrite-containing samples, which represents the characteristic signal of e-trapped in  $V_O$  [50–52]. Notably, the stronger ESR signal was observed with EcBFR-12Heme-800Fe and 52 H-EcBFR-800Fe as compared to other samples, suggesting that there are more unpaired electrons from surface  $V_O$ , which could endow the ferrihydrite nanoparticles with good electron conduction capability (Fig. 2e). Further photoluminescence spectra can be observed that the ferrihydrite nanoparticles exhibit an intense peak that gives a direct measurement of electron-hole recombination, proving their potential photocatalytic activity (Fig. 2f).

### 3.3. Photocatalytic performance towards $CO_2$ conversion by the above constructed hybrid ferritin complexes

The catalytic potency of the as-prepared sample EcBFR-12Heme-800Fe was evaluated with a 400 W high-pressure Hg lamp ( $\lambda = 425$  nm) as the light source because heme groups incorporated at the subunit interfaces have a maximum absorbance at  $\sim 420$  nm (Fig. 1b). It was found that when BNAH was used as an electron donor, formic acid was a major reduction product (88.2%) detected by high performance liquid chromatography (HPLC) with a very small amount of CO and  $CH_4$  detected by gas chromatography (GC) (Fig. 3a), indicating that the newly constructed hybrid protein platform exhibits high selectivity toward HCOOH.

To explore the above mechanism, effect of six different reaction conditions on photocatalytic  $CO_2$  reduction was investigated, and results

were displayed in Fig. 4b. One gram of the fabricated biocatalyst can catalyze  $CO_2$  to convert into around 840  $\mu\text{mol}$  of formic acid in the presence of BNAH upon irradiated with light ( $\lambda = 425$  nm) for 6 h, and this correspond to condition #1. In contrast, under the same conditions except for the absence of light (condition #2) or photosensitizer (condition #3) or photocatalyst (condition #4), there was almost no formic acid produced, suggesting that these three factors are required for  $CO_2$  photocatalytic reduction. Similarly, the absence of  $CO_2$  likewise results in no formic acid production under identical conditions, which represents condition #5. As expected, only the buffer solution plus the electron donor BNAH cannot directly reduce  $CO_2$  into formic acid, corresponding to condition #6. Thus, all these findings demonstrate that the observed production of formic acid is most likely stemmed from photocatalytic  $CO_2$  reduction by the constructed EcBFR-12Heme-800Fe hybrid protein nanocages with BNAH as the electron donor (Fig. 3a).

To decipher the great performance of the fabricated EcBFR-12Heme-800Fe sample in photocatalytic  $CO_2$  reduction, parallel tests were conducted by using free hemins mixed with EcBFR-2.5Heme-400Fe, EcBFR-2.5Heme-800Fe, 52 H-EcBFR-400Fe and 52 H-EcBFR-800Fe with a hemin/ferritin ratio of 12/1, respectively, rather than insertion into the subunit interfaces. Subsequently, the time-dependent production rate of formic acid as a function of irradiation time over four different samples was elucidated in Fig. 4b. In all experiments, BNAH was used as the electronic donor and formic acid was quantitated by HPLC on the basis of a calibration curve (Fig. S8). It was observed that both 52 H-EcBFR-400Fe plus hemin and 52 H-EcBFR-800Fe plus hemin generated

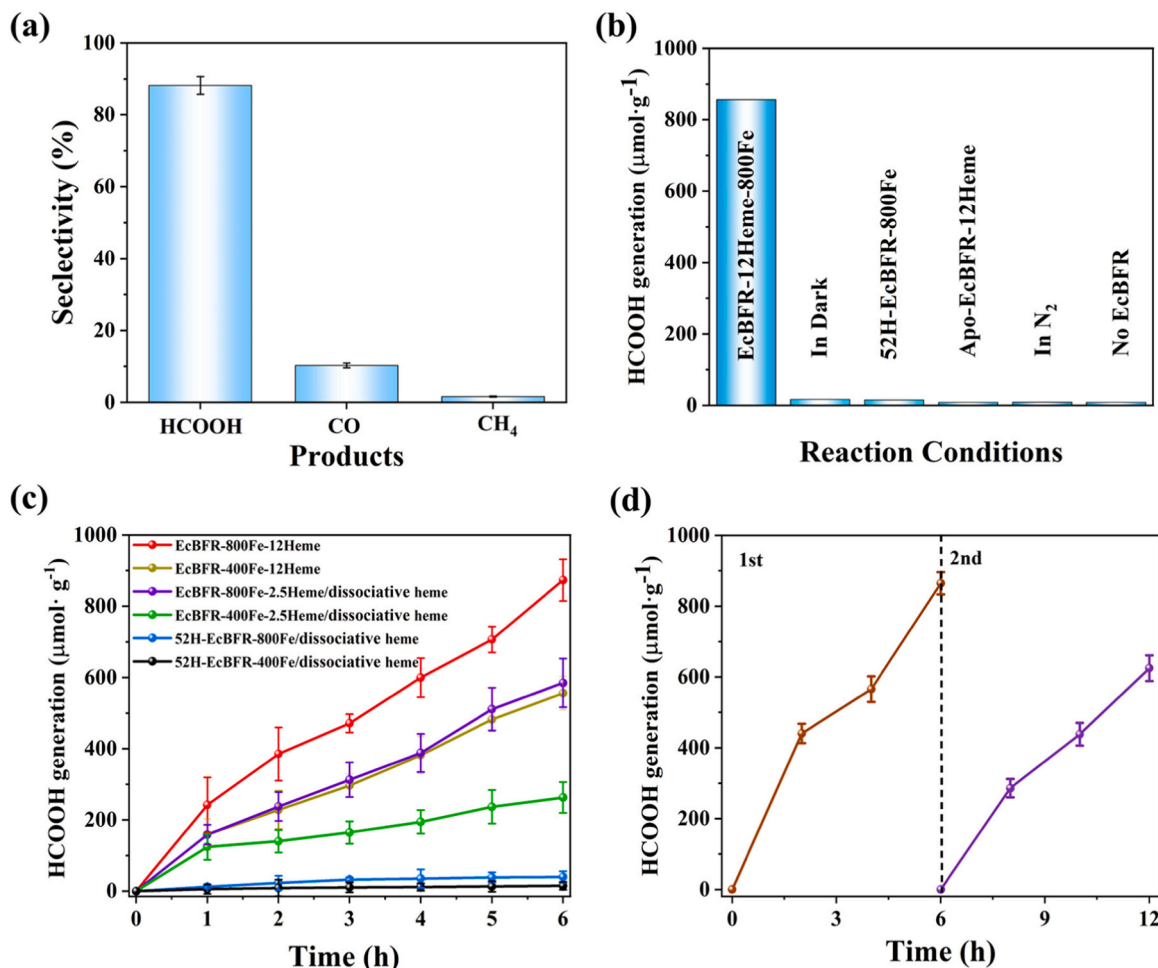


**Fig. 3.** Photocatalytic performance towards  $CO_2$  conversion by the constructed photocatalytic platform. (a) Selectivity of formic acid. (b) Effect of different reaction conditions on  $CO_2$  photoreduction. (c) Formic acid generation rates obtained for photocatalytic reduction of  $CO_2$  by different constructed hybrid complexes. (d) Recyclability of the EcBFR-12Heme-800Fe photocatalytic platform.

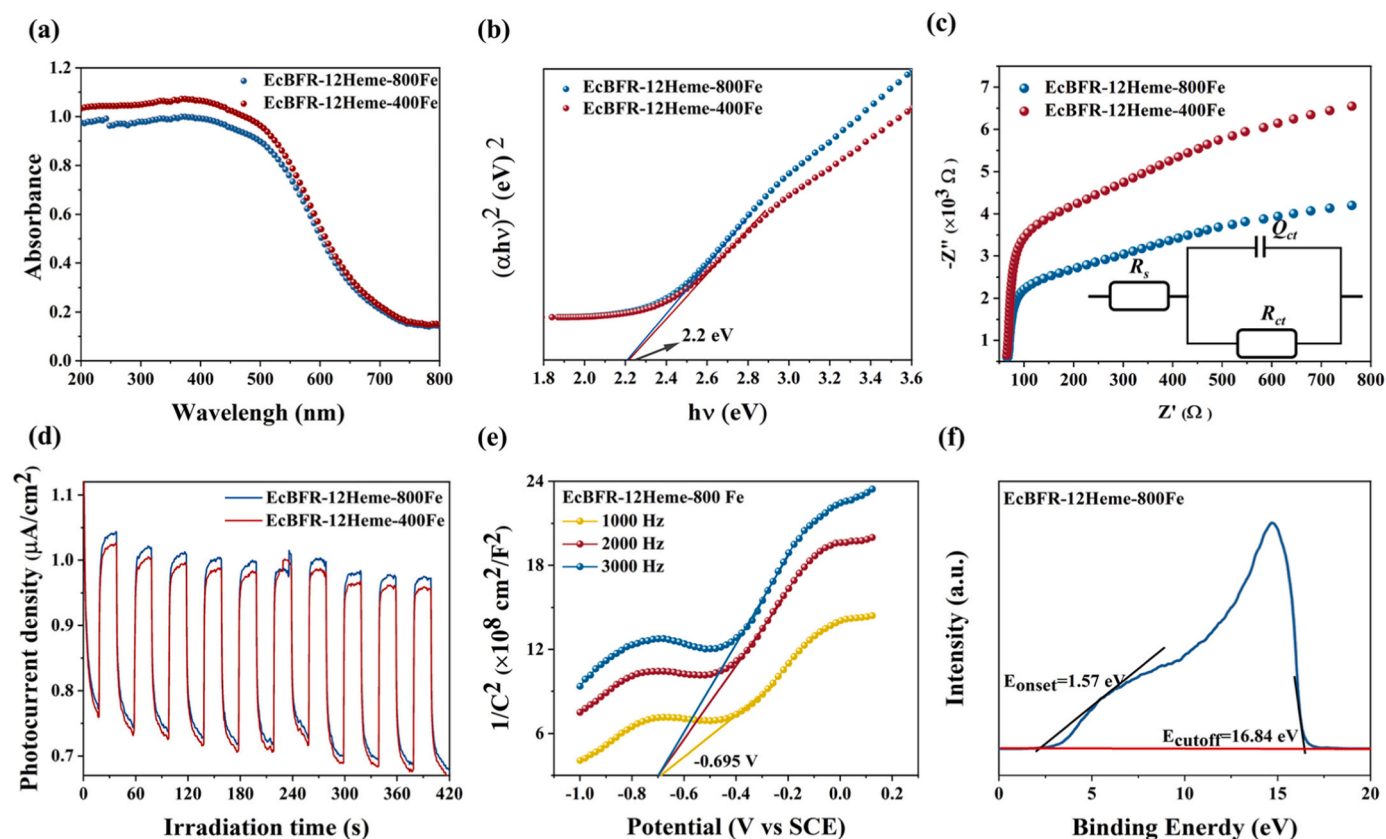


**Fig. 4.** Band structures and photoelectrochemical characters illustrating the possible photocatalytic mechanism of biosynthesized ferrihydrite nanoparticles. (a) UV-vis DRS. (b) Tauc plots. (c) Photocurrent response. (d) Nyquist plots. (Inset: The equivalent circuit used for fitting). (e) Mott-Schottky plots. (f) Ultraviolet photoelectron spectroscopy: binding energy to the Fermi level for EcBFR-12Heme-800Fe.

minimal formic acid, indicating that these two samples have limited photocatalytic activity in CO<sub>2</sub> reduction. Two samples EcBFR-2.5Heme-400Fe and EcBFR-2.5Heme-800Fe related to partial integration of heme into the intersubunit interfaces catalytically produced a certain amount of HCOOH. In contrast, under identical conditions, both EcBFR-12Heme-400Fe and EcBFR-12Heme-800Fe catalyzed the generation of the largest amount of formic acid at fixed ferrihydrite size, indicating that they have markedly strongest catalytic activity as compared to the above four simple mixture samples (Fig. 3b). The yield of formic acid increases almost linearly with reaction time within 6 h, indicative of good stability of these two samples in the CO<sub>2</sub> conversion process.

The large difference in the activity between two simply mixing samples and the samples (EcBFR-12Heme-400Fe and EcBFR-12Heme-800Fe) are believed to be derived from their different constructed modes: integration versus simply mixing. This is not surprising because such integration enables direct contact between the photosensitizer heme located at the subunit interfaces and the photocatalyst ferrihydrite nanoparticles within the inner cavity, thereby facilitating multiple electron transfer between them. These results emphasize the importance of simultaneous integration of the photosensitizer and the photocatalyst into a single protein molecule for photocatalytic CO<sub>2</sub> reduction. Additionally, it is worth noting that there is also the significant difference in the catalytic activity between the two samples (EcBFR-2.5Heme-400Fe and EcBFR-2.5Heme-800Fe) and their analogues (EcBFR-12Heme-400Fe and EcBFR-12Heme-800Fe), suggesting that the content of heme in the constructed hybrid ferritin nanocage likewise plays an important role in photocatalytic CO<sub>2</sub> reduction, and the larger amount of heme integrated into a single protein cage is more beneficial for light absorbance. Besides, the exterior surface of ferritin is composed of various functional groups that could interact with BNAH through noncovalent interactions characterized by UV-vis titration experiments, fluorescence

spectra and molecular docking (Fig. S9a-c). Results show that the amide group of BNAH located on the exterior surface of ferritin cage is close proximity to the incorporated photosensitizer heme, which might further facilitate the rapid electron transfer between the electron donor and the photosensitizer heme.

To elucidate effect of the size of ferrihydrite nanoparticles on photocatalytic CO<sub>2</sub> reduction, we compared the performance of EcBFR-12Heme-800Fe and EcBFR-12Heme-400Fe in converting CO<sub>2</sub> into formic acid with its analogue, and found that the EcBFR-12Heme-800Fe sample exhibited 1.5-fold stronger catalytic activity as compared to its analogue. As shown in Fig. 4c, the EcBFR-12Heme-800Fe sample generated about 840 μmol of formic acid by 6 h irradiation, while 550 μmol of formic acid was produced in the presence of EcBFR-12Heme-400Fe. Such large difference in the catalytic activity between EcBFR-12Heme-800Fe and EcBFR-12Heme-400Fe can be explained by their different apparent quantum yields during photocatalysis (Fig. S10). Thus, it appears that the constructed EcBFR hybrid protein nanocages with a larger core size have better performance in photocatalytic CO<sub>2</sub> reduction.

Since EcBFR-12Heme-800Fe exhibited the largest photocatalytic CO<sub>2</sub> reduction activity, we chose it as a model complex to evaluate the recyclability of the constructed hybrid protein complexes. After two cycles, the chemical state and morphology of ferrihydrite particles have not markedly changed with respect to the original materials (Fig. S11 and Fig. S12), however, the protein shell of EcBFR was damaged to a great extent (Fig. S13), resulting in significant loss in photocatalytic activity (Fig. 3d).

It was worth noting that prior to this study, ferrihydrite nanoparticles has not yet been explored as the catalyst in CO<sub>2</sub> photoreduction. In order to confirm the above observed photocatalytic reduction activity of the biosynthesized ferrihydrite nanoparticles, their band



structure and photoelectrochemical state were determined. Fig. 4a displays the UV absorption spectra of the ferrihydrite nanoparticles in the range 200–800 nm. Notably, ferrihydrite nanoparticles showed a wide absorption both in the UV light and visible light region. The estimated bandgap of ferrihydrite nanoparticles is about 2.21 eV by Kubelka-Munk function [53,54] as shown in Fig. 4b.

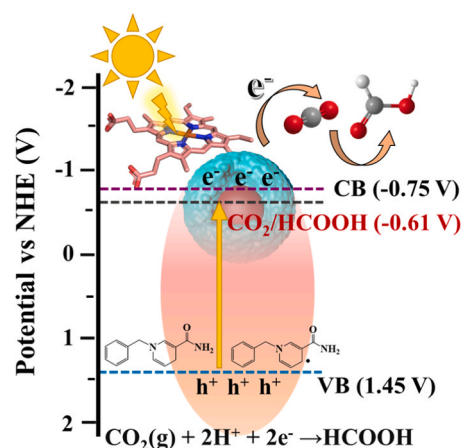
Charge transport and recombination action of the biosynthesized ferrihydrite were further monitored using electrochemical impedance spectra (EIS) and transient photocurrent responses. It is clearly seen that Nyquist plot has a single visible semicircle (Fig. 4c), suggesting an equivalent circuit model consisting of a couple of capacitances and resistances in parallel (Fig. 4c, inset). The charge transfer resistance at the electrode material/electrolyte interface ( $R_{ct}$ ) was evaluated using the radius of arc of Nyquist plot. It was observed that EcBFR-12Heme-800Fe photoanode (297  $\Omega$ ) possesses the lower electronic resistance than EcBFR-12Heme-400Fe (349.4  $\Omega$ ) as suggested by Nyquist plot with a smaller high-frequency semicircle, which is beneficial for accelerating separation and transfer of charge carriers in photocatalysis [55]. Accordingly, EcBFR-12Heme-800Fe affords a higher photo-current density than its analogue EcBFR-12Heme-400Fe (Fig. 4d), reaffirming the accelerated separation and movement of charge carriers in EcBFR-12Heme-800Fe with more iron content [56–58]. These results were coincided well with the above observed catalytic activity of these two samples. Followed Mott-Schottky curves with different frequencies of 1.0, 2.0 and 3.0 kHz were used to study the charge carrier behaviors of the biosynthesized photocatalysts (Fig. 4e). The positive slope determines the biosynthesized ferrihydrite nanoparticles as n-type in nature [59], which gives a good explanation of why the ferrihydrite nanoparticles exhibit CO<sub>2</sub> photoreduction activity.

To further reveal the corresponding catalytic mechanism, the Fermi level of ferrihydrite nanoparticles, the position of valence band and conduction band are determined by ultraviolet photoelectron spectroscopy (UPS) which is crucial to analyze the behavior of photogenerated electrons, and result is displayed in Fig. 5f. According to the UPS results, the valence band (VB), conduction band (CB) and Fermi levels were calculated to be 1.45 V, −0.75 V and −0.12 V, respectively, being in good agreement with the above UV-vis DRS and photoelectrochemical results. Based on the present findings, a possible mechanism of

photocatalytic CO<sub>2</sub> reduction by the biosynthesized ferrihydrite nanoparticles was illustrated in Scheme 2. Under irradiation with visible light, the photosensitizer heme undergoes excitation to allow electrons to be transferred from the VB of the ferrihydrite nanoparticles to their CB so that CO<sub>2</sub> can be converted into HCOOH in the presence of BNAH.

#### 3.4. Construction of 3D protein crystalline frameworks for higher recyclability

Although the above constructed EcBFR hybrid nanocages exhibited high photocatalytic CO<sub>2</sub> reduction activity, poor recyclability restricted their further applications, which is most likely due to relatively low stability of EcBFR nanocages as observed in Fig. S13. We envisioned that if 3D EcBFR crystalline frameworks were fabricated by using these individual hybrid protein nanocages as building blocks through self-assembly, the formed superarchitecture would improve the stability of each building block, thereby increasing the recyclability of the



**Scheme 2.** A possible mechanism of CO<sub>2</sub> photoconversion by biosynthesized ferrihydrite nanoparticles.

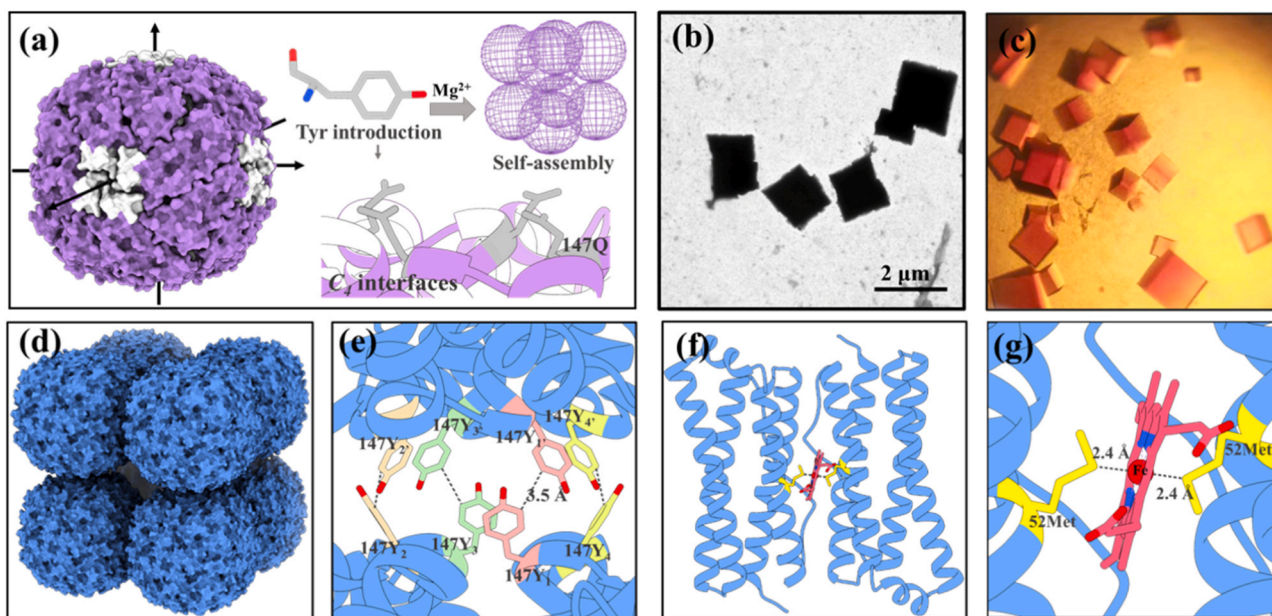


**Fig. 5.** Design and construction of 3D EcBFR crystalline frameworks for higher recyclability. (a) Design strategy for constructing 3D EcBFR crystalline frameworks. (b) The formation of 3D EcBFR crystalline frameworks in solution as shown by TEM. (c) Cubic-shaped crystals of EcBFR showing scarlet. (d) - (e) Illustration of the crystalline frameworks stacking in simple cubic manner through a group of 147Tyr-involved  $\pi$ - $\pi$  stacking interactions. (f) - (g) Illustration of heme incorporation into the C<sub>2</sub> interfaces of EcBFR in the crystalline frameworks through coordination bonds.

constructed EcBFR nanocages. However, the design of the crystalline frameworks was challenging because (1) the assembled EcBFR molecule is a relatively complicated protein with a rough surface; (2) the designed amino acid residues, which are responsible for the intermolecular interactions between two adjacent EcBFR molecules, should not be buried in the crevices on the surfaces, and instead, they protrude from the surface of ferritin nanocage; (3) the designed intermolecular interfaces should keep away from the site where the heme is located, otherwise they will interfere with the electron transfer from the electron donor BNAH and the photosensitizer.

After carefully analyzing the protein interfaces, we found that the design of the driving forces at the  $C_4$  interfaces of EcBFR satisfies these conditions. It would be expected that appropriate driving forces along the  $C_4$  symmetry axes of EcBFR nanocages would induce them to form 3D crystalline frameworks with a simple cubic structure on the basis of the fact that the octahedral symmetry of the EcBFR nanocage endows it with three  $C_4$  rotation axes that are perpendicular to each other (Fig. 5a). Here we chose  $\pi$ - $\pi$  stacking interactions as driving forces to design the intermolecular interactions because these noncovalent interactions are reversible, chemically tunable, and easily bioengineered. Upon inspection, Q147 lining the pores of the  $C_4$  axis nearby the exterior surface were deemed to be well suited for constructing a new motif for intermolecular  $\pi$ - $\pi$  stacking interactions (Fig. 5a).

To this end, we made another ferritin mutant named 147Y-EcBFR in which Gln147 in native EcBFR were mutated to Tyr (Fig. S14), and then this protein was purified to homogeneity by using the same method as wild-type ferritin. Just like its wild-type analogue EcBFR, native 147Y-EcBFR also appears scarlet in solution and has maximum absorption at 420 nm, a property similar to wild-type EcBFR (Fig. S15a-d). Since each 147Y-EcBFR molecule can bind to only 2.5 molecules of heme, so it was referred to as 147Y-EcBFR-2.5Heme. Subsequently, we prepared 147Y-EcBFR-12Heme where 12 molecules of hemin were integrated into each 147Y-EcBFR, by using identical method as EcBFR-12Heme. As expected, 147Y-EcBFR-12Heme exhibited a stronger absorbance at 420 nm (Fig. S15c). Similarly, 147Y-EcBFR-12Heme can likewise catalyze the fast oxidation of  $\text{Fe}^{2+}$  to  $\text{Fe}^{3+}$ , forming ferrihydrite particles within its inner cavity (Fig. S15e). By using the inherent enzymatic activity, we made another sample consisting of 800 iron per protein shell, which is called as 147Y-EcBFR-12Heme-800Fe.

Next, the assembly features of 147Y-EcBFR-12Heme-800Fe were investigated under different conditions. It was found that when 50 mM of  $\text{MgCl}_2$  was added to 2.0  $\mu\text{M}$  of 147Y-EcBFR-12Heme-800Fe solution in 50 mM MOPS, pH 7.5, excitingly, inerratic cubic-shaped superlattices were immediately formed in the solution at room temperature (Fig. 5b

and Fig. S16). To obtain more detailed assembly information of the superlattices, we solved their crystal structure by X-ray protein crystallography at a resolution of 2.8 Å with a  $P_{432}$  space group (Supplementary Tables 1 and 2). As designed, 147Y-EcBFR-12Heme-800Fe molecules hierarchically assembled into porous protein crystalline frameworks where two adjacent protein nanocages were bridged along the  $C_4$  symmetry axis by  $\pi$ - $\pi$  interactions coming from a group of designed 147Tyr residues (Fig. 5c-e). It was observed that each photosensitizer heme is located at the  $C_2$  interfaces of EcBFR through coordination with two Met52 residues (Fig. 5f-g). All these results demonstrate that 3D crystalline frameworks have been successfully constructed as designed.

Having built the 3D EcBFR crystalline frameworks in solution through the designed interactions, we move forward to photoreduction of  $\text{CO}_2$  under the same conditions as the individual hybrid EcBFR nanocage. Following analysis of the products after 6 h of reaction showed that formic acid was still the main reduction product of  $\text{CO}_2$ . It was also observed that the photocatalytic potency was slightly improved by such assembly. For example, about 874  $\mu\text{mol}$  of formic acid were produced by each ferritin nanocages occurring in the 3D EcBFR crystalline frameworks (Fig. 6a), while  $\sim 840$   $\mu\text{mol}$  of formic acid were generated by discrete EcBFR-12Heme-800Fe molecule (Fig. 3c). However, the 3D crystalline frameworks pronouncedly enhanced the recyclability of each EcBFR nanocage during photocatalytic  $\text{CO}_2$  reduction from two to five cycles (Fig. 6b), confirming our design. The most primary cause for the improvement of the recyclability could be attributed to the robustness of the designed 3D crystalline frameworks containing more  $\pi$ - $\pi$  stacking interactions.

#### 4. Conclusion

Photocatalytic  $\text{CO}_2$  reduction into chemicals and fuels has been considered as the most promising approach to solve the problems related to a great increase in  $\text{CO}_2$  emissions and energy deficiency, but most of the current photocatalytic reduction systems rely on precious metal photosensitizers and the harsh synthesis conditions of the photocatalysts. In this study, by taking advantage of chemically distinct interfaces of EcBFR, we designed an all-in-one photocatalytic reduction platform through hierarchical integration of the photosensitizer hemin and biocatalyst ferrihydrite into a single ferritin molecule in solution. Notably, the constructed all-in-one  $\text{CO}_2$  photocatalytic reduction platform exploited heme as a photosensitizer for the first time, which is able to selectively reduce  $\text{CO}_2$  to formic acid with high catalytic potency in an aqueous environment. Further designed  $\pi$ - $\pi$  stacking interactions

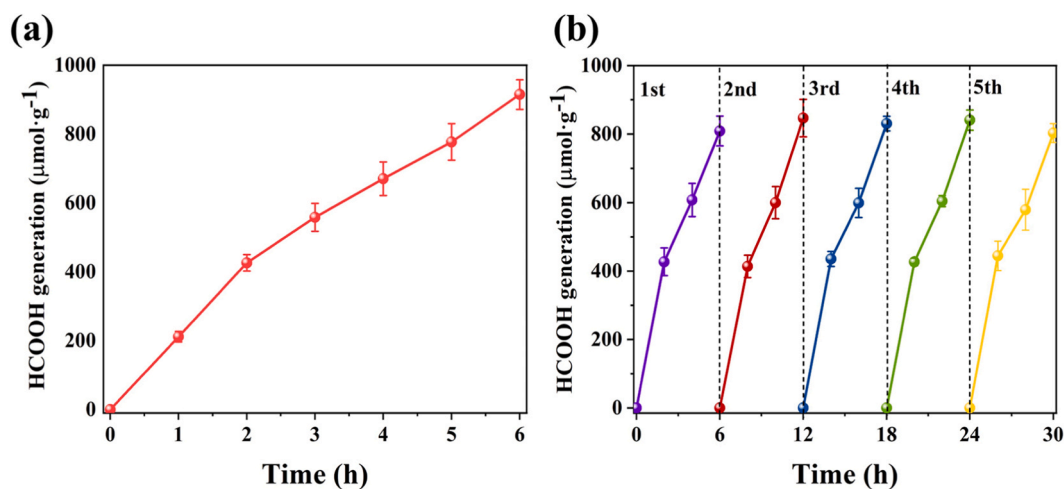


**Fig. 6.** Photocatalytic performance towards  $\text{CO}_2$  conversion by the constructed 3D crystalline frameworks. (a) The rate of formic acid generation for photocatalytic reduction of  $\text{CO}_2$  by EcBFR crystalline frameworks. (b) Recyclability of the 3D crystalline frameworks.

rendered the individual constructed EcBFR molecules to self-assemble into 3D protein crystalline frameworks in response to magnesium ion stimuli; consequently, the designed 3D frameworks obtain higher recyclability, and such property could be conducive to its durable application. Our constructed platform represents a simple as well as environmentally friendly platform for conversion of CO<sub>2</sub> into value-added chemicals with high efficiency under mild conditions.

### CRedit authorship contribution statement

**Ruiqi Zeng:** Resources, Methodology, Investigation, Formal analysis, Writing – original draft. **Xiaoxi Chang:** Resources, Methodology, Investigation, Formal analysis, Writing – original draft. **Tuo Zhang:** Supervision, Writing – review & editing. **Chenyan Lv:** Supervision, Writing – review & editing. **Jiachen Zang:** Supervision, Software. **Guanghua Zhao:** Conceptualization, Supervision, Writing – review & editing. All authors read and approved the final manuscript.

### Declaration of Competing Interest

The authors declare the following financial interests/personal relationships which may be considered as potential competing interests: vGuanghua Zhao reports financial support was provided by National Natural Science Foundation of China.

### Data Availability

Data will be made available on request.

### Acknowledgments

This work was supported by the National Natural Science Foundation of China (No. 32372320). The Shanghai Synchrotron Radiation Facility (SSRF) is especially acknowledged for beam time. We thank the staff from BL17U1/BL18U1 beamline of the National Center for Protein Sciences Shanghai (NCPSS) at Shanghai Synchrotron Radiation Facility (SSRF) for assistance during data collection.

### Accession codes

The atomic coordinates and structure factors in this study have been deposited in the Protein Data Bank under the accession PDB IDs: 8W8Z and 8WCU. Source data are provided with this paper.

### Appendix A. Supporting information

Supplementary data associated with this article can be found in the online version at doi:10.1016/j.apcatb.2023.123521.

### References

- [1] W.X. Zhang, Y. Yu, R.T. Huang, X.Y. Shi, Efficient photocatalytic reduction of CO<sub>2</sub> to CO Using NiFe<sub>2</sub>O<sub>4</sub>/N/C/SnO<sub>2</sub> derived from FeNi metal-organic framework, *ACS Appl. Mater. Interfaces* 13 (2021) 40571–40581.
- [2] W.B. Jiang, H.Y. Loh, B.Q.L. Low, H.J. Zhu, J.X. Low, J.Z.X. Heng, K.Y.T. Tang, Z. B. Li, X.J. Loh, E.Y. Ye, Y.J. Xiong, Role of oxygen vacancy in metal oxides for photocatalytic CO<sub>2</sub> reduction, *Appl. Catal. B: Environ.* 321 (2023), 122079.
- [3] M. Lu, M. Zhang, J. Liu, Y.F. Chen, J.P. Liao, M.Y. Yang, Y.P. Cai, S.L. Li, Y.Q. La, Covalent organic framework based functional materials: important catalysts for efficient CO<sub>2</sub> utilization, *Angew. Chem. Int. Ed.* 61 (2022), e202200003.
- [4] Y. Tamaki, O. Ishitani, Supramolecular photocatalysts for the reduction of CO<sub>2</sub>, *ACS Catal.* 7 (2017) 3394–3409.
- [5] Price Pressures on Metals. *Nature Catalysis*. 2(2019), 735.
- [6] J.W. Wang, F. Ma, T. Jin, P. He, Z.M. Luo, S. Kupfer, M. Karnahl, F. Zhao, Z. Xu, T. Jin, T. Lian, Y.L. Huang, L. Jiang, L.Z. Fu, G. Ouyang, X.Y. Yi, Homoleptic Al(III) photosensitizers for durable CO<sub>2</sub> photoreduction, *J. Am. Chem. Soc.* 145 (2023) 676–688.
- [7] A.E. Gallio, S.S.-P. Fung, A. Cammack-Najera, A.J. Hudson, E.L. Raven, Understanding the logistics for the distribution of heme in cells, *JACS Au* 1 (2021) 1541–1555.
- [8] A.M. Alsharabasy, A. Pandit, P. Farràs, Recent advances in the design and sensing applications of hemin/coordination polymer-based nanocomposites, *Adv. Mater.* 33 (2021), 2003883.
- [9] Y. Ling, L.X. Chen, J.X. Dong, N.B. Li, H.Q. Luo, A simple and rapid method for direct determination of Al(III) based on the enhanced resonance Rayleigh scattering of hemin-functionalized graphene-Al(III) system, *Spectrochim. Acta Part A: Mol. Biomol. Spectrosc.* 156 (2016) 22.
- [10] Y. Ye, J. Gao, H. Zhuang, H. Zheng, H. Sun, Y. Ye, X. Xu, X. Cao, Electrochemical gene sensor based on a glassy carbon electrode modified with hemin-functionalized reduced graphene oxide and gold nanoparticle-immobilized probe DNA, *Microchim. Acta* 184 (2017) 245.
- [11] Q. Chen, J. Chen, C. Gao, M. Zhang, J. Chen, H. Qiu, Hemin-functionalized WS<sub>2</sub> nanosheets as highly active peroxidase mimetics for label-free colorimetric detection of H<sub>2</sub>O<sub>2</sub> and glucose, *Analyst* 140 (2015) 2857.
- [12] F. Lebrun, A. Bazus, P. Dhulster, D. Guillochon, Solubility of heme in heme-iron enriched bovine hemoglobin hydrolysates, *J. Agric. Food Chem.* 46 (1998) 5017–5025.
- [13] Y. Lu, S.M. Berry, T.D. Pfister, Engineering novel metalloproteins: design of metal-binding sites into native protein scaffolds, *Chem. Rev.* 101 (2001) 3047.
- [14] P. Krishnamurthy, T. Xie, J. Schuetz, The role of transporters in cellular heme and porphyrin homeostasis, *Pharmacol. Ther.* 114 (2007) 345.
- [15] W. Gao, M. Chrzanowski, S. Ma, Metal-metalloporphyrin frameworks: a resurging class of functional materials, *Chem. Soc. Rev.* 43 (2014) 5841–5866.
- [16] Z.N. Zahran, E.A. Mohamed, A.A. Haleem, Y. Naruta, Efficient solar-assisted CO<sub>2</sub> reduction using a cofacial iron porphyrin dimer catalyst integrated into a P-Cu<sub>2</sub>O<sub>4</sub> photocathode, *Chem. -A Eur. J.* 24 (2018) 10606–10611.
- [17] H. Takeda, O. Ishitani, Development of efficient photocatalytic systems for CO<sub>2</sub> reduction using mononuclear and multinuclear metal complexes based on mechanistic studies, *Coord. Chem. Rev.* 254 (2010) 346–354.
- [18] B. Zhang, L. Sun, Artificial photosynthesis: opportunities and challenges of molecular catalysts, *Chem. Soc. Rev.* 48 (2019) 2216–2264.
- [19] H. Yin, Z. Zhang, T. Lu, Ordered integration and heterogenization of catalysts and photosensitizers in metal-covalent-organic frameworks for boosting CO<sub>2</sub> photoreduction, *Acc. Chem. Res.* 56 (2023) 2676–2687.
- [20] W. Zhu, C. Zhang, Q. Li, L. Xiong, R. Chen, X. Wan, Z. Wang, W. Chen, Z. Denga, Y. Peng, Selective reduction of CO<sub>2</sub> by conductive MOF nanosheets as an efficient co-catalyst under visible light illumination, *Appl. Catal. B: Environ.* 238 (2018) 339–345.
- [21] R. Bhardwaj, T. Sharma, D.D. Nguyen, C. Cheng, S.S. Lam, C. Xia, A.K. Nadda, Integrated catalytic insights into methanol production: Sustainable framework for CO<sub>2</sub> conversion, *J. Environ. Manag.* 289 (2021), 112468.
- [22] Y. Ma, X. Wang, Y. Jia, X. Chen, H. Han, C. Li, Titanium dioxide-based nanomaterials for photocatalytic fuel generations, *Chem. Rev.* 114 (2014) 9987–10043.
- [23] C. Lv, X. Zhang, Y. Liu, T. Zhang, H. Chen, J. Zang, B. Zheng, G. Zhao, Redesign of protein nanocages: the way from 0D, 1D, 2D to 3D assembly, *Chem. Soc. Rev.* 50 (2021) 3957–3989.
- [24] M.A. Canady, S.B. Larson, J. Day, A. McPherson, Crystal structure of turnip yellow mosaic virus, *Nat. Struct. Biol.* 3 (1996) 771–781.
- [25] F. Bou-Abdallah, The iron redox and hydrolysis chemistry of the ferritins, *Biochim. Et. Biophys. Acta* 1800 (2010) 719–731.
- [26] M. Uchida, S. Kang, C. Reichardt, K. Harlen, T. Douglas, The ferritin superfamily: supramolecular templates for materials synthesis, *Biochim. Et. Biophys. Acta Gen. Subj.* 1800 (2010) 834–845.
- [27] X. Chang, C. Lv, G. Zhao, A dual function of ferritin (animal and plant): its holo form for iron supplementation and apo form for delivery systems, *Ann. Rev. Food Sci. Technol.* 14 (2023) 113–133.
- [28] S.G. Wong, R. Abdulqadir, N.E. Le Brun, G.R. Moore, A.G. Mauk, Fe-haem bound to *Escherichia coli* bacterioferritin accelerates iron core formation by an electron transfer mechanism, *Biochem. J.* 444 (2012) 553–560.
- [29] S.G. Wong, S.A.L. Tom-Yew, A. Lewin, N.E. Le Brun, G.R. Moore, M.E.P. Murphy, A.G. Mauk, Structural and mechanistic studies of a stabilized subunit dimer variant of *Escherichia coli* bacterioferritin identify residues required for core formation, *J. Biol. Chem.* 284 (2009) 18873–18881.
- [30] Z. Otwinowski, W. Minor, Processing of X-ray diffraction data collected in oscillation mode, *Methods Enzymol.* 276 (1997) 307.
- [31] L.W. Hung, J.J. Headd, P.H. Zwart, V. Chen, J.S. Richardson, T.C. Terwilliger, P. D. Adams, P.V. Afonine, G.J. Kapral, R. Oeffner, I.W. Davis, N.W. Moriarty, D. C. Richardson, R.W. Grosse Kunstleve, A.J. McCoy, N. Echols, G. Bunkoczi, R. J. Read, PHENIX: a comprehensive Python-based system for macromolecular structure solution, *Acta Crystallogr. Sect. D.* 66 (2010) 213–221.
- [32] P. Emsley, B. Lohkamp, W.G. Scott, K. Cowtan, Features and development of Coot, *Acta Crystallogr. Sect. D.* 66 (2010) 486–501.
- [33] E.F. Pettersen, T.D. Goddard, C.C. Huang, G.S. Couch, D.M. Greenblatt, E.C. Meng, T.E. Ferrin, U.C.S.F. Chimera-a, visualization system for exploratory research and analysis, *J. Comput. Chem.* 25 (2004) 1605–1612.
- [34] Y. Kuramochi, A. Satake, Porphyrins acting as photosensitizers in the photocatalytic CO<sub>2</sub> reduction reaction, *Catalysts* 13 (2023) 282.
- [35] S.G. Wong, J.C. Grigg, N.E. Le Brun, G.R. Moore, M.E.P. M, A.G. Mauk, The B-type channel is a major route for iron entry into the ferroxidase center and central cavity of bacterioferritin, *J. Biol. Chem.* 290 (2015) 3732–3739.
- [36] C.B. Bie, B. Zhu, F. Xu, L. Zhang, J. Yu, In situ grown monolayer N-doped graphene on CdS hollow spheres with seamless contact for photocatalytic CO<sub>2</sub> reduction, *Adv. Mater.* 31 (2019), 1902868.



- [37] J.C. Zang, H. Chen, G.H. Zhao, F.D. Wang, F.Z. Ren, Ferritin cage for encapsulation and delivery of bioactive nutrients: from structure, property to applications, *Crit. Rev. Food Sci. Nutr.* 57 (2017) 3673–3683.
- [38] S.L. Zhang, J.C. Zang, H. Chen, M.L. Li, C.S. Xu, G.H. Zhao, The size flexibility of ferritin nanocage opens a new way to prepare nanomaterials, *Small* 13 (2017), 1701045.
- [39] R. Yang, L.L. Chen, S. Yang, C.Y. Lv, X.J. Leng, G.H. Zhao, 2D square arrays of protein nanocages through channel-directed electrostatic interactions with poly( $\alpha$ , L-lysine), *Chem. Commun.* 50 (2014) 2879–2882.
- [40] C. Li, X. Fu, X. Qi, X. Hu, N.D. Chasteen, G. Zhao, Protein association and dissociation regulated by ferric ion: a novel pathway for oxidative deposition of iron in pea seed ferritin, *J. Biol. Chem.* 284 (2009) 16743–16751.
- [41] P.D. Hempstead, S.J. Yewdall, A.R. Fernie, D.M. Lawson, P.J. Artymiuk, D.W. Rice, G.C. Ford, P.M. Harrison, Comparison of the three-dimensional structures of recombinant human H and horse L ferritins at high resolution, *J. Mol. Biol.* 268 (1997) 424–448.
- [42] X. Yang, Y. Chen-Barrett, P. Arosio, N.D. Chasteen, Reaction paths of iron oxidation and hydrolysis in horse spleen ferritin and recombinant human ferritins, *Biochemistry* 37 (1998) 9763–9770.
- [43] J. Lee, N.D. Chasteen, G. Zhao, G.C. Papaefthymiou, S.M. Gorun, Deuterium structural effects in inorganic and bioinorganic aggregates, *J. Am. Chem. Soc.* 124 (2002) 3042–3049.
- [44] N.D. Chasteen, P.M. Harrison, Mineralization in ferritin: an efficient means of iron storage, *J. Struct. Biol.* 126 (1999) 182–194.
- [45] F.M. Michel, L. Ehm, S.M. Antao, R.L. Penn, P.J. Chupas, G. Liu, D.R. Strongin, M. A.A. Schoonen, B.L. Phillip, J.B. Parise, The structure of ferrihydrite, a nanocrystalline material, *Science* 316 (2007) 1726–1729.
- [46] J.L. Jambor, J.E. Dutrizac, Occurrence and constitution of natural and synthetic ferrihydrite, a widespread iron oxyhydroxide, *Chem. Rev.* 98 (1998) 2549–2585.
- [47] Y. Guyodo, P. Saintavit, M.A. Arrio, C. Carvallo, R.L. Penn, J.J. Erbs, B. S. Forsberg, G. Morin, F. Maillot, F. Lagroix, P. Bonville, F. Wilhelm, A. Rogalev, X-ray magnetic circular dichroism provides strong evidence for tetrahedral iron in ferrihydrite, *Geochim. Geophys. Geosyst.* 13 (2012) Q06Z44.
- [48] D. Carta, A. Casula, A. Corrias, A. Falqui, G. Navarra, G. Pinna, Structural and magnetic characterization of synthetic ferrihydrite nanoparticles, *Mater. Chem. Phys.* 113 (2009) 349–355.
- [49] F. Maillot, G. Morin, Y. Wang, D. Bonnin, P. Ildefonse, C. Chaneac, G. Calas, New insight into the structure of nanocrystalline ferrihydrite: EXAFS evidence for tetrahedrally coordinated iron(III), *Geochim. Et. Cosmochim. ACTA* 75 (2011) 2708–2720.
- [50] F. Chen, Z.Y. Ma, L.Q. Ye, T.Y. Ma, T.R. Zhang, Y.H. Zhang, H.W. Huang, Macroscopic spontaneous polarization and surface oxygen vacancies collaboratively boosting CO<sub>2</sub> photoreduction on BiOIO<sub>3</sub> single crystals, *Adv. Mater.* 32 (2020), 1908350.
- [51] S.D. Yang, H.Y. Li, H.M. Li, H.M. Li, W.S. Qi, Q. Zhang, J. Zhu, P. Zhao, L. Chen, Rational design of 3D carbon nitrides assemblies with tunable nano-building blocks for efficient visible-light photocatalytic CO<sub>2</sub> conversion, *Appl. Catal. B-Environ.* 316 (2022), 121612.
- [52] F.L. Yang, X. Bao, P. Li, X.W. Wang, G.Z. Cheng, S.L. Chen, W. Luo, Boosting hydrogen oxidation activity of Ni in alkaline media through oxygen-vacancy-rich CeO<sub>2</sub>/Ni heterostructures, *Angew. Chem. -Int. Ed.* 58 (2019) 14179–14183.
- [53] W. Fu, X. Xu, W. Wang, J. Shen, M. Ye, In-situ growth of NiFe<sub>2</sub>O<sub>4</sub>/2D MoS<sub>2</sub> P-N heterojunction immobilizing palladium nanoparticles for enhanced visible-light photocatalytic activities, *ACS Sustain. Chem. Engine* 6 (2018) 8935–8944.
- [54] W. Zhang, Y. Yu, R. Huang, X. Shi, Efficient photocatalytic reduction of CO<sub>2</sub> to CO using NiFe<sub>2</sub>O<sub>4</sub>@N/C/SnO<sub>2</sub> derived from FeNi metal-organic framework, *ACS Appl. Mater. Interfaces* 13 (2021) 40571–40581.
- [55] G. Liu, Y. Zhao, N. Li, R. Yao, M.H. Wang, Y. Wu, F. Zhao, J.P. Li, Ti-doped hematite photoanode with surface phosphate ions functionalization for synergistic enhanced photoelectrochemical water oxidation, *Electrochim. Acta* 307 (2019) 197–205.
- [56] G.J. Chen, F. Wei, Z.R. Zhou, B. Su, C. Yang, X.F. Lu, S.B. Wang, X.C. Wang, Phase junction crystalline carbon nitride nanosheets modified with CdS nanoparticles for photocatalytic CO<sub>2</sub> reduction, *Sustain. Energy Fuels* 7 (2022) 381–388.
- [57] Z.P. Xie, W.B. Wang, X.T. Ke, X. Cai, X. Chen, S.B. Wang, W. Lin, X.C. Wang, A heptazine-based polymer photocatalyst with donor-acceptor configuration to promote exciton dissociation and charge separation, *Appl. Catal. B-Environ.* 325 (2023), 122312.
- [58] B. Su, M. Zheng, W. Lin, X.F. Lu, D.Y. Luan, S.B. Wang, X.W. Lou, S-scheme Co<sub>9</sub>S<sub>8</sub>@Cd<sub>0.8</sub>Zn<sub>0.2</sub>S-DETA hierarchical nanocages bearing organic CO<sub>2</sub> Activators for photocatalytic syngas production, *Adv. Energy Mater.* 13 (2023) 202203290.
- [59] L. Chen, S.D. Yang, Q. Zhang, J. Zhu, P. Zhao, Rational design of (001)-faceted TiO<sub>2</sub> nanosheet arrays/graphene foam with superior charge transfer interfaces for efficient photocatalytic degradation of toxic pollutants, *Sep. Purif. Technol.* 265 (2021), 118444.